Enabling Intrinsic Antiferroelectricity in Two-dimensional $NbOCl_2$: Molecular Dynamics Simulations based on Deep Learning Interatomic Potential

Jiawei Mao(毛嘉伟)[1], Yinglu Jia(贾瑛璐)[2], Gaoyang Gou(缑高阳)[1*], Shi Liu(刘仕)[3,4*], and Xiao Cheng Zeng[5*]

[1]*Frontier Institute of Science and Technology, State Key Laboratory of Electrical Insulation and Power Equipment, Xi'an Jiaotong University, Xi'an 710049, China*
[2]*Department of Chemistry, University of Nebraska-Lincoln, Lincoln NE68588, USA*
[3]*Department of Physics, School of Science and Research Center for Industries of the Future, Westlake University, Hangzhou 310030, China*
[4]*Institute of Natural Sciences, Westlake Institute for Advanced Study, Hangzhou 310024, China*
[5]*Department of Materials Science and Engineering, City University of Hong Kong, Hong Kong 999077, China*

(Received 23 September 2025; accepted manuscript online 24 November 2025)

Compared to the well-studied two-dimensional (2D) ferroelectricity, the appearance of 2D antiferroelectricity is much rarer, where local dipoles from the nonequivalent sublattices within 2D monolayers are oppositely oriented. Using $NbOCl_2$ monolayer with competing ferroelectric (FE) and antiferroelectric (AFE) phases as a 2D material platform, we demonstrate the emergence of intrinsic antiferroelectricity in $NbOCl_2$ monolayer under experimentally accessible shear strain, along with new functionality associated with electric field-induced AFE-to-FE phase transition. Specifically, the complex configuration space accommodating FE and AFE phases, polarization switching kinetics, and finite temperature thermodynamic properties of 2D $NbOCl_2$ are all accurately predicted by large-scale molecular dynamics simulations based on deep learning interatomic potential model. Moreover, room temperature stable antiferroelectricity with low polarization switching barrier and one-dimensional collinear polarization arrangement is predicted in shear-deformed $NbOCl_2$ monolayer. The transition from AFE to FE phase in 2D $NbOCl_2$ can be triggered by a low critical electric field, leading to a double polarization–electric (P–E) loop with small hysteresis. A new type of optoelectronic device composed of AFE-$NbOCl_2$ is proposed, enabling electric "writing" and nonlinear optical "reading" logical operation with fast operation speed and low power consumption.

DOI: 10.1088/0256-307X/43/1/010703 CSTR: 32039.14.0256-307X.43.1.010703

Spontaneous symmetry breaking in ferroic materials with certain order parameters can activate unique material properties and functional responses.[1] Compared to ferroelectric (FE) materials with spontaneous ferroelectricity and the breaking of spatial inversion symmetry, antiferroelectric (AFE) materials possess rich structural phase transition features and new application prospects, such as thermal switching,[2] dielectric energy storage,[3] electrocaloric effects,[4] and electrostrictive effects[5] that are less accessible in their FE counterparts.[6] However, antiferroelectricity has more stringent structural and energetic requirements than ferroelectricity. Specifically, the compensating net polarizations in AFE materials originate from the opposite local dipole arrangement within nonequivalent sublattices, which are usually accompanied by unit-cell doubling or structural modulation.[6] Moreover, the presence of a low-energy FE phase in proximity to the stable AFE phase is also required. The competing AFE and FE phases are both associated with structural instabilities inherent from the same high-symmetry reference structure.[7] Most importantly, electric field-induced AFE-to-FE phase transition is a key aspect of unique functional responses and application potential for antiferroelectricity.[8]

The stringent requirement of antiferroelectricity also applies to two-dimensional (2D) van der Waals (vdW) layered materials, where intrinsic 2D antiferroelectricity is much rarer than 2D ferroelectricity. In fact, ferroelectricity are widely reported and extensively investigated in various 2D FE materials with displacive ferroelectricity (e.g., $CuInP_2S_6$,[9,10] SnTe,[11] α-In_2Se_2,[12,13] and single-element Bi-monolayer[14,15]) and sliding ferroelectricity (e.g., 1T'-WTe_2,[16] 1T'-ReS_2,[17] 3R-MoS_2,[18] 3R-BN,[19] γ-GaSe,[20] and γ-InSe[21]). While antiferroelectricity is reported in very limited cases that are often termed as 2D "multi-polar" materials.[22] For example, in the experimentally synthesized 2D AFE materials such as α-GeSe[23] and $CuBiP_2Se_6$,[24] each of their monolayers has a net FE polarization; antiferroelectricity appears in those even-numbered multilayers with antiparallel monolayer-polarization arrangement. In this context, intrinsic 2D antiferroelectricity able to persist in monolayer limit (breaking even-layer-number requirement) has rarely

*Corresponding authors. Email: gougaoyang@mail.xjtu.edu.cn; liushi@westlake.edu.cn; xzeng26@cityu.edu.hk
© 2026 Chinese Physical Society and IOP Publishing Ltd. All rights, including for text and data mining, AI training, and similar technologies, are reserved.

been realized.

Combining the high-throughput screening of the vdW layered materials database and first-principles calculations, we identified $NbOX_2$ (X = Cl, Br, and I) as a new group of 2D FE materials.[25] Especially owing to its stable in-plane ferroelectricity, large polarization magnitude,[26] and giant second harmonic generation (SHG) response,[27,28] $NbOCl_2$ becomes an ideal system to explore 2D ferroelectricity and second-order optical nonlinearity. Besides, unit-cell doubling induced by Peierls distortion between Nb^{4+} cations of $NbOCl_2$ naturally meets the structural requirement for antiferroelectricity. Moreover, the metastable AFE phase in proximity to the stable FE phase is predicted for 2D $NbOCl_2$ in both monolayer and multilayer structural forms.[25] Alternating the energy sequence between the competing FE and AFE phases by a proper control parameter[7] will make intrinsic antiferroelectricity accessible in $NbOCl_2$ monolayer. However, simulation of antiferroelectricity within AFE-$NbOCl_2$ calls for accurately predicting kinetic and thermodynamic properties associated with structural transitions between AFE and FE phases,[29,30] which is beyond the capacity of zero-temperature DFT calculations. The limitations of DFT calculations can be well addressed by the deep learning interatomic potential (DP) model, where the interatomic potential is accurately trained using DFT datasets based on deep neural network algorithms.[31] In fact, DP model and associated DP molecular dynamics (DPMD) simulations can model domain-wall motion and polarization switching kinetics over large space- and time-scales for sliding FEs.[32,33] Therefore, reproducing complex configuration space and accurately predicting intrinsic 2D ferroelectricity as well as antiferroelectricity of $NbOCl_2$ become feasible by performing large-scale molecular dynamics (MD) simulations based on DP model with quantum accuracy.

From the crystal structure point of view, 2D vdW layered $NbOCl_2$ manifests as a structural derivative of ABO_3 perovskite without A-site cation and out-of-plane connectivity, where the 2D structural framework of the $NbOCl_2$ monolayer is composed of NbO_2Cl_4 octahedrons with mixed corner- and edge-sharing connectivity along two planar directions. As displayed in Fig. 1(a), Nb-Nb Peierls distortion occurs along the Nb-Cl-Nb bonding direction, while the polar displacement of Nb cations relative to octahedral centers along the Nb-O-Nb direction can lead to in-plane polarization. Besides, the low-lying AFE phase also presents in the $NbOCl_2$ monolayer via opposite displacement of Nb cations from two neighboring octahedrons (i.e., nonequivalent Nb sublattices). FE and AFE phases are determined to be the ground state and metastable structural phases for free-standing $NbOCl_2$ monolayer, respectively;[25] both of which are associated with zone-center structural instabilities out of high-symmetry paraelectric (PE) reference.

Owing to the negligible interlayer electronic coupling,[27] the energetic and structural properties of 2D $NbOCl_2$ are nearly independent of the number of monolayers included. We therefore develop a first-principles-derived DP model[31,34,35] for the $NbOCl_2$ monolayer [see Section I and Fig. S1 in Supplementary Materials (SM)] to simulate the intrinsic ferroelectricity and potential antiferroelectricity of 2D $NbOCl_2$. Our well-trained DP model can predict static properties, such as energies, atomic forces, and phonon dispersion with satisfactory accuracy comparable to DFT results (Section II and Figs. S2–S4 in SM). The accuracy of the DP model is also validated by

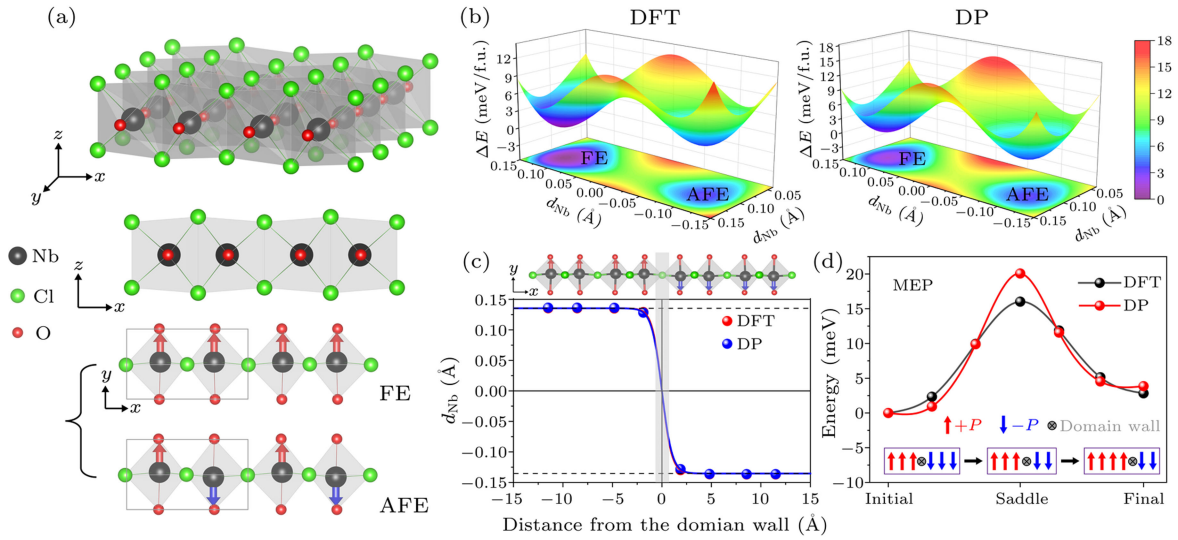

Fig. 1. (a) Crystal structure for the 2D $NbOCl_2$ monolayer. Nb polar displacements in the ground-state stable FE and metastable AFE phases along the $\pm y$ direction are indicated by red and blue arrows, respectively. Unit cells of FE- or AFE-$NbOCl_2$ monolayer are marked as black squares. (b) The PES (in meV·f.u.$^{-1}$) for relative displacement of two neighboring Nb cations within the free-standing $NbOCl_2$ monolayer, calculated by DFT and DP model. Both FE and AFE states within PES are identified. (c) In the optimized 180° FE domain-wall configuration of the $NbOCl_2$ monolayer, variation of d_{Nb} as a function of distance (r) away from the domain wall simulated by DFT (marked in red color) and DP model (in blue), respectively. The 180° domain wall with sharp width is shown in gray area. (d) The MEP and energy barriers for polarization switching within the FE-$NbOCl_2$ monolayer predicted by DFT and DP model. The schematic diagram for domain-wall motion induced polarization switching scenario is also provided.

reproducing the DFT potential energy surface (PES) for free-standing $NbOCl_2$ monolayer, which refers to the variation of system energy as a function of Nb polar displacement (d_{Nb}) between two nonequivalent Nb sublattices. Both d_{Nb} magnitudes and energy sequences for the stable FE and metastable AFE states within PES are well captured by the DP model [Fig. 1(b) and Table S1 of the SM].

Besides the static properties, the accuracy in predicting the kinetic processes of $NbOCl_2$ monolayer, such as energy pathways and barriers associated with domain wall motion and polarization switching by the DP model has also been evaluated. As d_{Nb} is restricted along one planar axis but completely forbidden along the other, formation of a 180° domain wall between oppositely oriented FE single domains has been predicted [25] and experimentally validated [26] in 2D $NbOCl_2$. Shown in Fig. 1(c) is the variation of d_{Nb} as a function of position (r) away from the domain wall, where d_{Nb}–r profiles predicted by DFT and DP model are nearly identical, yielding a sharp domain wall width as small as 2 Å (Section III of the SM). The atomically thin domain wall along the Nb-Cl-Nb direction of $NbOCl_2$ can be rationalized by the flat soft phonon that is nearly dispersionless along the corresponding reciprocal path [Fig. S4(b) in SM]. Similar relations between flat soft phonons and atomically thin domain-wall widths have also been established in hafnia FEs. [36,37] Specifically, sharp domain-wall widths can facilitate the polarization switching kinetics of 2D $NbOCl_2$ through the motion of the domain wall. As shown in Fig. 1(d), the transition from the initial to final state across a saddle point along the simulated minimum energy pathway (MEP) resembles the domain-wall motion induced polarization switching. The MEP associated with polarization switching predicted by the DP model based on the NEB method agrees well with DFT results, except that the DP model slightly overestimates the energy barrier by 4 meV. Overall, the DP model can well reproduce the static and kinetic properties of the free-standing $NbOCl_2$ monolayer obtained from DFT calculations, establishing a solid foundation for accurately predicting its thermodynamic properties at finite temperatures.

In the experiment, the stable ferroelectricity and strong optical nonlinearity arising from structural noncentrosymmetry have been detected in 2D $NbOCl_2$ at room temperature. [27,38–40] However, *in situ* experimental characterizations of Nb polar displacement with atomic resolution remain challenging; the microscopic mechanism regarding temperature-induced phase transition in 2D $NbOCl_2$ is still unknown. Based on the DP model, we can perform finite-temperature MD simulations of $NbOCl_2$ at the mesoscopic scale, establishing the relation between macroscopic ferroelectricity and microscopic mechanisms [Fig. 2(a)]. The statistically averaged $\bar{d}_{Nb}$ serves as an order parameter to quantify the polarization magnitude, while the probability distribution of d_{Nb} [Fig. 2(b)] and real space tracing of d_{Nb} on each lattice grid within the $NbOCl_2$ monolayer [Figs. 2(c)–2(e)] as a function of temperature can provide more atomic information regarding the phase transition mechanism. DPMD simulations are performed on the FE phase of $NbOCl_2$ monolayer with exactly the same d_{Nb} on each lattice grid [Fig. 2(c)].

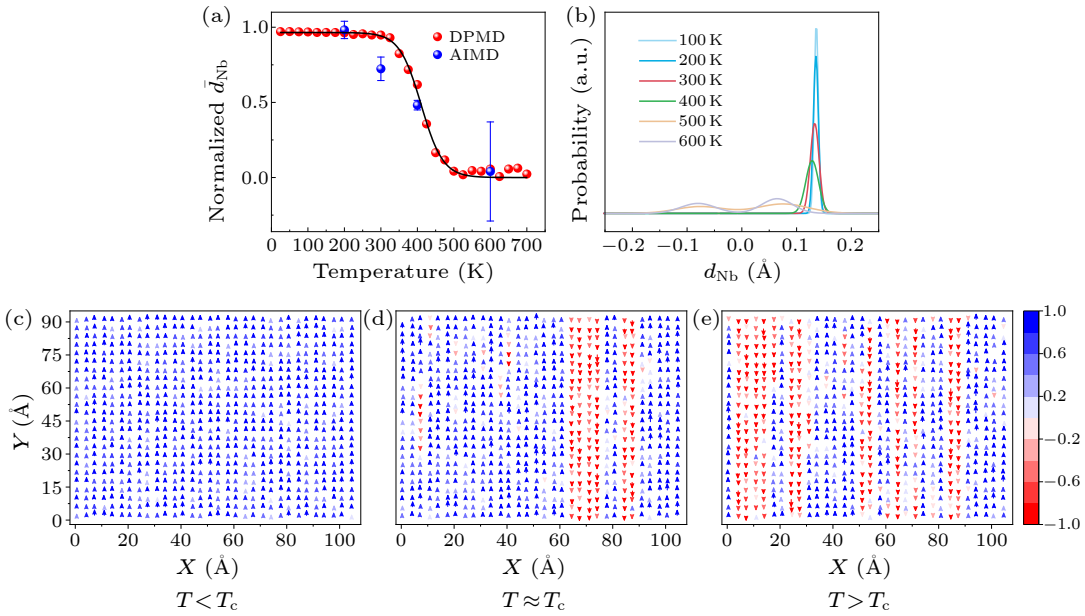

Fig. 2. Temperature-induced FE–PE phase transition in the free-standing $NbOCl_2$ monolayer. (a) Temperature-dependent statistically averaged $\bar{d}_{Nb}$ normalized to its zero-temperature value, predicted by *ab initio* MD (AIMD) and DPMD simulations, respectively. The large error bars are due the strong thermal fluctuations during AIMD simulations performed on the $NbOCl_2$ monolayer with a small supercell. (b) The probability distributions of d_{Nb} at different temperatures. (c)–(e) Snapshots of the FE-$NbOCl_2$ monolayer obtained from DPMD simulations performed at temperatures below, around, and above T_c. Each $NbOCl_2$ monolayer configuration contains 16×24 Nb octahedrons, where d_{Nb} is indicated by colored arrows with different magnitudes. Reversal of polarization orientations is indicated by changing blue arrows into red along the entire Nb lattice columns.

FE-to-PE phase transition occurs when the temperature approaches the Curie temperature ($T_c \approx 396$ K), accompanied by a sudden drop in $\bar{d}_{Nb}$ magnitude [Fig. 2(a)] and a shift in the positions of d_{Nb} probability distribution peaks towards lower values [Fig. 2(b)], as well as reversing the orientations of d_{Nb} for the entire column along the polar axis [Fig. 2(d)]. Above T_c, the $NbOCl_2$ monolayer enters the PE state: each grid has a non-zero d_{Nb}, and the overall random orientation of d_{Nb} for individual columns leads to $\bar{d}_{Nb} = 0$ [Fig. 2(e)]. Within the PE state, distributions of d_{Nb} correspond to two broad probability peaks with opposite peak positions. The deviation of T_c between DPMD predictions and experimental measurements[40] is about 50 K. Meanwhile, the magnitudes of $\bar{d}_{Nb}$ predicted by DPMD simulations are in good agreement with ensemble averaged $\bar{d}_{Nb}$ from AIMD simulations performed at selected temperatures.[25] Moreover, compared to large thermal fluctuations during AIMD simulations, more statistically reliable results can be produced by DPMD simulations performed on ultra-large supercells, where the supercell size effect can be well eliminated.[41,42]

Based on zero-temperature DFT calculations for the free-standing $NbOCl_2$ monolayer, the metastable AFE phase and stable FE phase are close in energy ($\Delta E = 3$ meV·f.u.$^{-1}$), but antiferroelectricity has never been detected in 2D $NbOCl_2$ by experiment. In fact, even if we perform finite-temperature DPMD simulations on the AFE-$NbOCl_2$ monolayer, the AFE phase still cannot be stabilized at room temperature. Instead, the $NbOCl_2$ monolayer adopts an FE state with oppositely oriented FE single domains and a non-zero $\bar{d}_{Nb}$ magnitude (Fig. S5 in SM). Therefore, an alternative control parameter rather than temperature should be employed to stabilize the AFE phase of $NbOCl_2$.

The proper control parameter (e.g., compositional substitution or elastic strain) that can alter the energy sequence of FE and AFE phases may also trigger the structural transition between the two phases.[7] As for 2D $NbOCl_2$, the intrinsic antiferroelectricity can be stabilized by experimentally accessible shear strain. Figure 3(a) displays the variation of system energies for FE, AFE, and PE phases of the $NbOCl_2$ monolayer as a function of the applied shear strain, whose magnitude refers to the radian value of the angle change induced by shear strain between two planar axes of the $NbOCl_2$ monolayer. Without shear strain, free-standing $NbOCl_2$ monolayer has a strong preference towards the ground-state FE phase. The alternation of energy sequence between FE and AFE phases occurs when the magnitude of shear strain applied to the $NbOCl_2$ monolayer is above 2%, which is readily achievable in experiments.[43] The mechanism underlying the shear strain-stabilized AFE phase can be revealed by

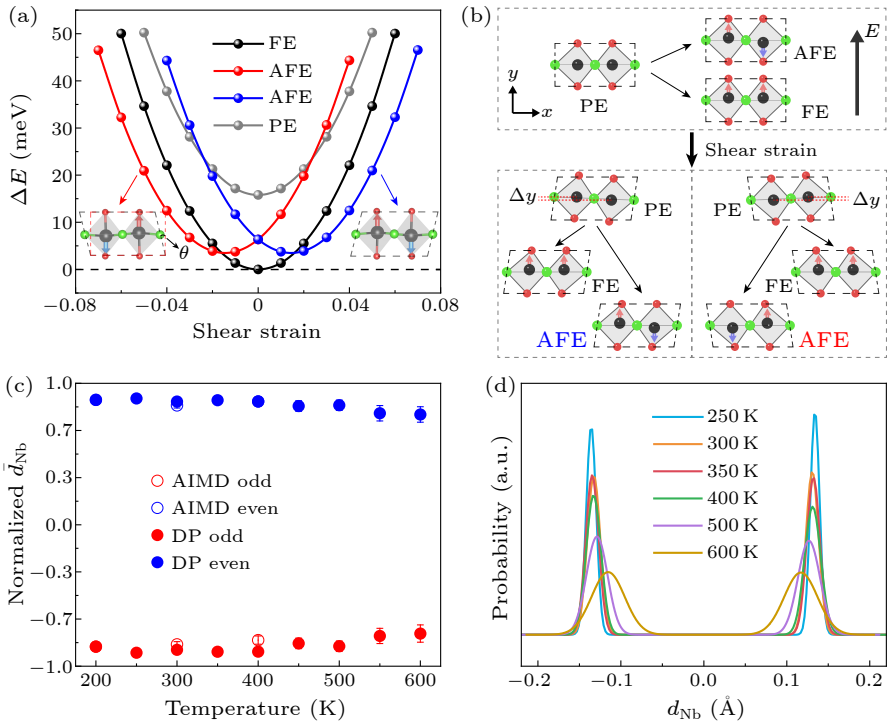

Fig. 3. (a) The variation of system energies for the $NbOCl_2$ monolayer in FE, AFE, and PE phases as a function of the applied shear strain predicted by DFT calculations. The energy of the free-standing (strain-free) FE-$NbOCl_2$ monolayer is set as energy zero. The inset illustrates how 2D lattices of the $NbOCl_2$ monolayer are deformed under shear strain. (b) Schematic diagram for stabilization of antiferroelectricity within the $NbOCl_2$ monolayer by shear strain, where shifting the positions of two neighboring Nb cations away from the same atomic plane naturally stabilizes the AFE phase with ↓↑ or ↑↓ d_{Nb} arrangement. (c) Variation of the normalized $\bar{d}_{Nb}$ from two inequivalent Nb sublattices (odd and even Nb lattice columns) within the AFE-$NbOCl_2$ monolayer as a function of temperature, predicted by AIMD and DPMD simulations. (d) Probability distributions of d_{Nb} within the AFE-$NbOCl_2$ monolayer at different temperatures. In the AFE-$NbOCl_2$ monolayer, $\bar{d}_{Nb}$ from two nonequivalent Nb sublattices are in nearly equal magnitudes but with opposite signs.

a schematic diagram displayed in Fig. 3(b). For free-standing PE-$NbOCl_2$, two neighboring Nb cations are located in the same Nb-Cl-Nb atomic plane. The softer FE unstable phonon mode within the PE phase [Fig. S4(b) of the SM] is responsible for the stable FE and metastable AFE phases of the free-standing $NbOCl_2$ monolayer. When PE-$NbOCl_2$ is shear deformed above a certain magnitude, two neighboring Nb cations are shifted away from the same atomic plane [indicated by Δy in Fig. 3(b)]. Such a shear-strain-driven geometry effect will reduce the energy term associated with dipole–dipole interactions between Nb cations.[25] Moreover, owing to the 1D collinear d_{Nb} arrangement and small FE–AFE energy difference, the neighboring Nb cations shifted relatively upwards or downwards have a tendency to display polar displacement along $+y$ or $-y$ axis, rendering the metastable AFE phase with $\downarrow\uparrow$ or $\uparrow\downarrow$ polarization arrangement as the ground-state stable structure for the $NbOCl_2$ monolayer under moderate shear strain.

The above prediction regarding the shear strain induced FE-to-AFE transition is made by zero temperature DFT calculations. In order to access intrinsic antiferroelectricity from 2D $NbOCl_2$ through experiments, the thermal stability of AFE-$NbOCl_2$ should be evaluated by finite temperature MD simulations. To this end, following a similar procedure for free-standing $NbOCl_2$ monolayer, we also develop the DP model for the $NbOCl_2$ monolayer under 5% shear strain. The accuracy of the DP model for shear-strained $NbOCl_2$ monolayer is also validated by reproducing DFT results, such as system energy, atomic forces, PES, energy difference between FE and AFE phases, as well as phonon dispersions (Figs. S6, S7 and Table S1 in SM). Finite temperature properties of AFE-$NbOCl_2$ are then examined by performing DPMD simulations on strained $NbOCl_2$ monolayer. Different from the FE phase, $\bar{d}_{\mathrm{Nb}}$ from two nonequivalent Nb sublattices (odd and even Nb lattice columns) is employed as the order parameter to quantitatively describe the AFE phase. The AFE-$NbOCl_2$ monolayer characterizes the collinear and antiparallel arrangement of d_{Nb} between two nonequivalent Nb sublattices ($\downarrow\uparrow$ and $\uparrow\downarrow$, see Fig. S8 in SM), so that statistically averaged $\bar{d}_{\mathrm{Nb}}$ from odd and even columns are in nearly the same magnitudes but with opposite signs [Fig. 3(c)], leading to two symmetric and sharp d_{Nb} probability distribution peaks [Fig. 3(d)]. Moreover, antiferroelectricity in strained $NbOCl_2$ monolayer can persist above room temperature, where $|\bar{d}_{\mathrm{Nb}}|$ at 300 K decreases slightly from the low-temperature values and shifts positions of d_{Nb} probability peaks towards lower amplitudes. Once again, $\bar{d}_{\mathrm{Nb}}$ predicted by DPMD simulations is nearly coincident with ensemble-averaged $\bar{d}_{\mathrm{Nb}}$ obtained from AIMD simulations, which convincingly demonstrates stable room temperature antiferroelectricity in strained $NbOCl_2$ monolayer. Moreover, we also perform DPMD simulations on AFE-$NbOCl_2$ monolayer, cooling down from high-temperature PE (disordered AFE) phase to room temperature AFE phase. The formation of an AFE domain wall and local polarization fluctuation across the domain wall are also predicted (see $\downarrow\downarrow\uparrow\uparrow$ polar arrangement in Fig. S9 of the SM).

Besides the structural characteristics, simulating the electric field induced AFE-to-FE phase transition can provide the most definitive indication of antiferroelectricity.[7] Thanks to the predictive capacity of the DP model, we can simulate the hysteresis loop of AFE-$NbOCl_2$ monolayer under the applied electric field that can directly resemble experimental measurements. During the DPMD simulations, an electric field E_β applied along the β direction of $NbOCl_2$ monolayer is simulated by adding extra forces on atom i: $F_{i,\alpha} = \sum_\beta Z^*_{i,\alpha\beta} E_\beta$, where $Z^*_{i,\alpha\beta}$ are the Born effective charge (BEC) tensors for atom i. As BEC in $NbOCl_2$ is nearly independent of structural phases (see Table S2 in SM), fixed BECs are therefore employed for DPMD simulations. Shown in Fig. 4(a) is our simulated hysteresis loop by recording changes in $\bar{d}_{\mathrm{Nb}}$ with respect to electric field E applied along the polar y axis of strained $NbOCl_2$ monolayer, obtained from DPMD simulations performed around room temperature. The simulated double hysteresis loop of strained $NbOCl_2$ monolayer is a characteristic feature of intrinsic antiferroelectricity. Without an external electric field, the strained $NbOCl_2$ monolayer crystallizes in the AFE phase [stage i of Fig. 4(b)]. The $\bar{d}_{\mathrm{Nb}}$ magnitude increases gradually when $NbOCl_2$ is under positive electric poling. The AFE-to-FE transition occurs at stage ii, where d_{Nb} along the entire lattice column starts to reverse its direction. When the electric field is above 0.016 V/Å, $NbOCl_2$ enters the FE state with saturated polarization (stage iii). The reversible FE-to-AFE phase transition occurs at stage iv. Two critical electric fields responsible for AFE-to-FE and FE-to-AFE transitions are close in magnitude ($E_{\mathrm{AFE-FE}} = 0.006$ *vs* $E_{\mathrm{AFE-FE}} = 0.01$ V/Å), leading to a double P–E loop with small hysteresis. It is noted that P–E loops with more obvious hysteresis are predicted by DPMD simulations performed at lower temperatures (Fig. S10 in SM). Therefore, the overall small hysteresis and low critical electric fields in AFE-$NbOCl_2$ around room temperature are associated with a small polarization switching barrier to be overcome by the external electric field.[44]

In experiments, rich research efforts have been dedicated to engineering SHG responses of $NbOCl_2$.[39,40,45] However, electric control of the optical nonlinearity in 2D $NbOCl_2$ has never been realized. Specifically, after switching the polarization of FE-$NbOCl_2$ by an external electric field, $\pm P$ states with opposite polarization orientations characterize the same SHG responses.[27] With the emergence of intrinsic antiferroelectricity, a new scenario for engineering the optical nonlinearity of $NbOCl_2$ can be realized [Fig. 4(c)]. As-prepared $NbOCl_2$ nanoflakes can be deposited on a hard nanocone through experiments. The strain can be transferred from the hard nanocone to $NbOCl_2$ by interfacial shear deformation.[46] Alternatively, shear strain may also be applied to 2D $NbOCl_2$ via in-plane shear force during the mechanical exfoliation process[47] or thin-film epitaxy growth approach.[48] The amplitude of effective shear strain on $NbOCl_2$ can be determined by *in situ* Raman characterization.[43] Antiferroelectricity appears when 2D $NbOCl_2$ is under certain shear deformation.

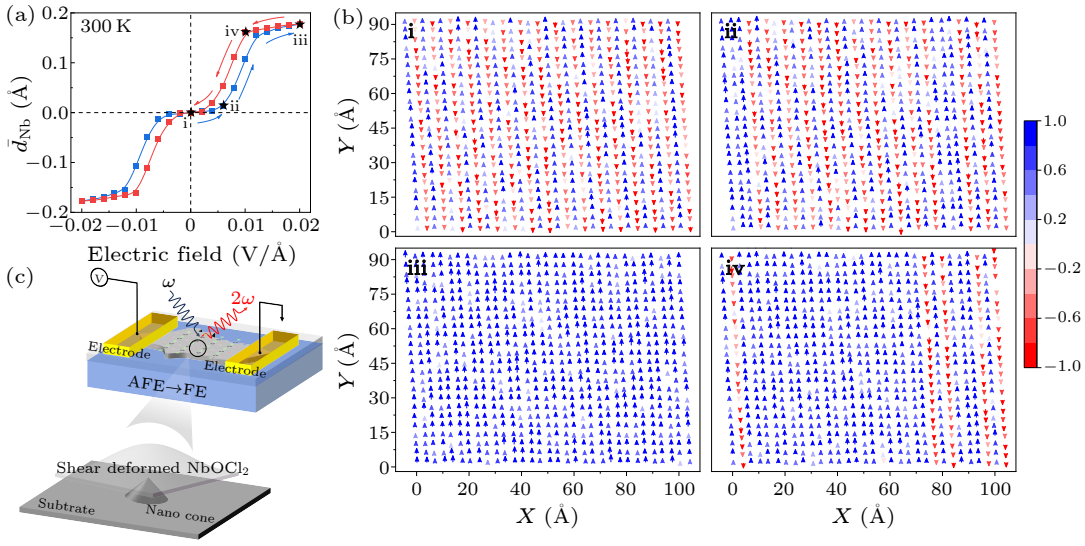

Fig. 4. Electric-field-induced AFE-to-FE phase transition in $NbOCl_2$ monolayer under 5% shear strain. (a) Double hysteresis loop by recording the variation of statistically averaged $\bar{d}_{Nb}$ as a function of electric field E applied along the polar y axis, obtained from DPMD simulations performed around room temperature. (b) Tracing of d_{Nb} within the $NbOCl_2$ monolayer for four prototypical snapshot configurations along the hysteresis loop. At stages i and iii, the strained-$NbOCl_2$ monolayer is in AFE and FE phases, respectively. The reversible transition between FE and AFE phases occurs at stages ii and iv when $NbOCl_2$ is under the low critical field ($E_c < 0.01$ V/Å). (c) Schematic diagram for electric control of optical nonlinearity in 2D $NbOCl_2$. Tuning the centrosymmetric AFE phase free of SHG signal into an FE phase with a giant SHG response can be realized in shear-deformed $NbOCl_2$ nanoflake by electric poling.

The transition from the centrosymmetric AFE phase free of SHG signal into FE-$NbOCl_2$ with a giant SHG response by electric poling enables the electric control of second-order optical nonlinearity in 2D $NbOCl_2$. Moreover, compared to the experimentally synthesized 2D AFE materials (e.g., α-GeSe[23] and $CuBiP_2Se_6$[24]), antiferroelectricity of strained $NbOCl_2$ is able to persist up to monolayer limit. Therefore, combining the small hysteresis and low critical field during AFE-to-FE phase transition, electric "writing" and nonlinear optical "reading" in an optoelectronic device composed of AFE-$NbOCl_2$ with low power consumption and fast operation speed can be expected.

In summary, a first-principles-derived DP model was developed for 2D $NbOCl_2$ with intrinsic ferroelectricity and antiferroelectricity. Large-scale DPMD simulations were performed to reveal the macroscopic properties and microscopic mechanisms regarding the temperature and electric field driven phase transitions of $NbOCl_2$. For free-standing $NbOCl_2$ monolayer with in-plane ferroelectricity, the DP model can well predict its energy landscape, atomically sharp domain wall, and Curie temperature with sufficient accuracy. Besides the well-studied 2D ferroelectricity, accessing the previously overlooked antiferroelectricity in $NbOCl_2$ via strain engineering approach has also been demonstrated. The room temperature stable antiferroelectricity was predicted in 2D $NbOCl_2$ monolayer under experimentally accessible shear strain, according to MD simulations based on the iteratively refined DP model. Especially owing to the unique collinear arrangement of local polarizations restricted along one planar axis and low polarization switching barrier, transition from AFE phase free of SHG response to FE phase with giant SHG intensity can be triggered by a low critical electric field, rendering a double P–E loop with small hysteresis. Based on comprehensive simulations performed on $NbOCl_2$ with competing FE and AFE ordering, our work not only demonstrates a reliable approach for enabling 2D antiferroelectricity but also provides a new strategy for electric control of optical nonlinearity in $NbOCl_2$ via electric field induced AFE-to-FE phase transition.

Acknowledgements. This work was supported by the National Natural Science Foundation of China (Grant No. 11574244 for G.Y.G.), the XJTU Research Fund for AI Science (Grant No. 2025YXYC011 for G.Y.G.), and the Hong Kong Global STEM Professorship Scheme (for X.C.Z.). We acknowledge Prof. Bin Xu from Soochow University for helpful discussion and Hefei Advanced Computing Center for computational support.

References

[1] Ramesh R and Spaldin N A 2007 *Nat. Mater.* **6** 21
[2] Pan H, Zhu M, Banyas E, Alaerts L, Acharya M, Zhang H, Kim J, Chen X, Huang X, Xu M, Harris I, Tian Z, Ricci F, Hanrahan B, Spanier J E, Hautier G, LeBeau J M, Neaton J B, and Martin L W 2024 *Nat. Mater.* **23** 944
[3] Acharya M, Banyas E, Ramesh M, Jiang Y, Fernandez A, Dasgupta A, Ling H, Hanrahan B, Persson K, Neaton J B, and Martin L W 2022 *Adv. Mater.* **34** 2105967
[4] Mischenko A S, Zhang Q, Scott J F, Whatmore R W, and Mathur N D 2006 *Science* **311** 1270
[5] Zhang S, Kounga A B, Jo W, Jamin C, Seifert K, Granzow T, Rödel J, and Damjanovic D 2009 *Adv. Mater.* **21** 4716
[6] Si Y, Zhang T, Liu C, Das S, Xu B, Burkovsky R G, Wei X K, and Chen Z 2024 *Prog. Mater. Sci.* **142** 101231
[7] Rabe K M 2013 *Functional Metal Oxides: New Science and Novel Applications* (Wiley) p. 221

[8] Reyes-Lillo S E, Garrity K F, and Rabe K M 2014 *Phys. Rev. B* **90** 140103
[9] Liu F, You L, Seyler K L, Li X, Yu P, Lin J, Wang X, Zhou J, Wang H, He H, Pantelides S T, Zhou W, Sharma P, Xu X, Ajayan P M, Wang J, and Liu Z 2016 *Nat. Commun.* **7** 12357
[10] Li W, Liu H, and Zeng H 2025 *Chin. Phys. Lett.* **42** 057501
[11] Chang K, Liu J, Lin H, Wang N, Zhao K, Zhang A, Jin F, Zhong Y, Hu X, Duan W, Zhang Q, Fu L, Xue Q K, Chen X, and Ji S H 2016 *Science* **353** 274
[12] Ding W, Zhu J, Wang Z, Gao Y, Xiao D, Gu Y, Zhang Z, and Zhu W 2017 *Nat. Commun.* **8** 14956
[13] Xiao J, Zhu H, Wang Y, Feng W, Hu Y, Dasgupta A, Han Y, Wang Y, Muller D A, Martin L W, Hu P, and Zhang X 2018 *Phys. Rev. Lett.* **120** 227601
[14] Gou J, Bai H, Zhang X, Huang Y L, Duan S, Ariando A, Yang S A, Chen L, Lu Y, and Wee A T S 2023 *Nature* **617** 67
[15] Wang Y, Lei Z, Zhang J, Tao X, Hua C, and Lu Y 2023 *Chin. Phys. Lett.* **40** 117102
[16] Fei Z, Zhao W, Palomaki T A, Sun B, Miller M K, Zhao Z, Yan J, Xu X, and Cobden D H 2018 *Nature* **560** 336
[17] Wan Y, Hu T, Mao X, Fu J, Yuan K, Song Y, Gan X, Xu X, Xue M, Cheng X, Huang C, Yang J, Dai L, Zeng H, and Kan E 2022 *Phys. Rev. Lett.* **128** 067601
[18] Bian R, He R, Pan E, Li Z, Cao G, Meng P, Chen J, Liu Q, Zhong Z, Li W, and Liu F 2024 *Science* **385** 57
[19] Wang L, Qi J, Wei W, Wu M, Zhang Z, Li X, Sun H, Guo Q, Cao M, Wang Q, Zhao C, Sheng Y, Liu Z, Liu C, Wu M, Xu Z, Wang W, Hong H, Gao P, Wu M, Wang Z J, Xu X, Wang E, Ding F, Zheng X, Liu K, and Bai X 2024 *Nature* **629** 74
[20] Li W, Zhang X, Yang J, Zhou S, Song C, Cheng P, Zhang Y Q, Feng B, Wang Z, Lu Y, Wu K, and Chen L 2023 *Nat. Commun.* **14** 2757
[21] Sui F, Jin M, Zhang Y, Qi R, Wu Y N, Huang R, Yue F, and Chu J 2023 *Nat. Commun.* **14** 36
[22] Bai H, Su X, Zhang Q, Uher C, Tang X, and Wu J 2022 *Nano Lett.* **22** 4083
[23] Guan Z, Zhao Y, Wang X, Zhong N, Deng X, Zheng Y, Wang J, Xu D, Ma R, Yue F, Cheng Y, Huang R, Xiang P, Wei Z, Chu J, and Duan C 2022 *ACS Nano* **16** 1308
[24] Yang D, Lin Y, Meng W, Wang Z, Li H, Li C, Zhang Z, Zhang Q, You J, Wang J, Yu T, Li Y, Miao W, Zhen W, Xue F, Fei R, and Sun L 2025 *Adv. Mater.* **37** 2419204
[25] Jia Y, Zhao M, Gou G, Zeng X C, and Li J 2019 *Nanoscale Horiz.* **4** 1113
[26] Liu C, Zhang X, Wang X, Wang Z, Abdelwahab I, Verzhbitskiy I, Shao Y, Eda G, Sun W, Shen L, and Loh K P 2023 *ACS Nano* **17** 7170
[27] Guo Q, Qi X Z, Zhang L, Gao M, Hu S, Zhou W, Zang W, Zhao X, Wang J, Yan B, Xu M, Wu Y K, Eda G, Xiao Z, Yang S A, Gou H, Feng Y P, Guo G C, Zhou W, Ren X F, Qiu C W, Pennycook S J, and Wee A T S 2023 *Nature* **613** 53
[28] Xuan F, Lai M, Wu Y, and Quek S Y 2024 *Phys. Rev. Lett.* **132** 246902
[29] Zhang H, Thong H C, Bastogne L, Gui C, He X, and Ghosez P 2024 *Phys. Rev. B* **110** 054109
[30] Shi Y, Wang R, Zhong Z, Wu Y, Liu S, Si L, and He R 2025 *Mater. Genome Eng. Adv.* **3** e70012
[31] Zhang L, Han J, Wang H, Car R, and E W 2018 *Phys. Rev. Lett.* **120** 143001
[32] Ke C, Liu F, and Liu S 2025 *Phys. Rev. Lett.* **135** 046201
[33] Shi Y, Gao Y, Wang H, Zhang B, Zhong Z, and He R 2025 *Phys. Rev. B* **112** 035421
[34] Zhang L, Han J, Wang H, Saidi W, Car R, and E W 2018 *Advances in Neural Information Processing Systems* (Curran Associates, Inc.) **31**
[35] Zhang Y, Wang H, Chen W, Zeng J, Zhang L, Wang H, and E W 2020 *Comput. Phys. Commun.* **253** 107206
[36] Lee H J, Lee M, Lee K, Jo J, Yang H, Kim Y, Chae S C, Waghmare U, and Lee J H 2020 *Science* **369** 1343
[37] Qi Y and Rabe K M 2025 *Phys. Rev. Lett.* **135** 046101
[38] Abdelwahab I, Tilmann B, Zhao X, Verzhbitskiy I, Berté R, Eda G, Wilson W L, Grinblat G, Menezes L D S, Loh K P, and Maier S A 2023 *Adv. Opt. Mater.* **11** 2202833
[39] Chu L, Gao S, Li Z, Zhu H, Liu W, Jia Y, and Chen F 2024 *Nano Lett.* **24** 15457
[40] Ye L, Zhou W, Huang D, Jiang X, Guo Q, Cao X, Yan S, Wang X, Jia D, Jiang D, Wang Y, Wu X, Zhang X, Li Y, Lei H, Gou H, and Huang B 2023 *Nat. Commun.* **14** 5911
[41] Wu J, Zhang Y, Zhang L, and Liu S 2021 *Phys. Rev. B* **103** 024108
[42] Wu J, Bai L, Huang J, Ma L, Liu J, and Liu S 2021 *Phys. Rev. B* **104** 174107
[43] Jiang J, Chen Z, Hu Y, Xiang Y, Zhang L, Wang Y, Wang G C, and Shi J 2021 *Nat. Nanotechnol.* **16** 894
[44] Xu B, Íñiguez J, and Bellaiche L 2017 *Nat. Commun.* **8** 15682
[45] Jia M, Chen J, Wu X, Qu X, and Huang M 2025 *Appl. Phys. Lett.* **126** 013104
[46] Dai Z, Liu L, and Zhang Z 2019 *Adv. Mater.* **31** 1805417
[47] Liang J, Yang D, Xiao Y, Chen S, Dadap J I, Rottler J, and Ye Z 2023 *Nano Lett.* **23** 7228
[48] Guo J, Tao L, Gu J, Lang W, Guo J, Nan C, Chen C, Zhang Q, Du S, and Ma J 2025 *Adv. Mater.* e10844